Supplementary Information

Origin and Predictive Principle for Selective Products of Electrocatalytic Carbon Dioxide Reduction

Lele Gong[1], Xiaowei Wang[2], Rahman Daiyan[3], Xiaofeng Zhu[3], Joshua Leverett,[3] Zhiyao Duan[4], Lipeng Zhang*[1], Rose Amal[3], Liming Dai[3], Zhenhai Xia*[3]

[1] College of Chemical Engineering, Beijing University of Chemical Technology, Beijing, 100029, China

[2] Department of Materials Science and Engineering, University of North Texas, Denton, TX 76203, USA

[3] Australian Carbon Materials Centre (A-CMC), School of Chemical Engineering, The University of New South Wales, Sydney, NSW, 2052, Australia

[4] School of Materials Science and Engineering, Northwestern Polytechnical University, Xi'an, 710072, China

Supplementary Notes:

Note 1. Gibbs Free Energy and Adsorption Energy Calculation

In carbon dioxide reduction reaction (CO_2RR), the first elementary step is adsorption of gaseous reactant, CO_2, on the surface of catalysts, which is one of the critical steps to determine catalytic mechanism and catalytic activity. Thus, in a neutral or acidic environment, CO_2RR to CO product is assumed to proceed a four-step reaction:

$$* + \mathrm{CO_{2(g)}} \rightarrow * \mathrm{COO} \qquad (S1)$$

$$* \mathrm{COO} + \mathrm{H^+} + e^- \rightarrow * \mathrm{COOH} \qquad (S2)$$

$$* \mathrm{COOH} + \mathrm{H^+} + e^- \rightarrow * \mathrm{CO} + \mathrm{H_2O_{(l)}} \qquad (S3)$$

$$* \mathrm{CO} \rightarrow * + \mathrm{CO_{(g)}} \qquad (S4)$$

where * refers to the active site on the surface of catalysts, subscripts *g* and *l* stand for the gas and liquid phases, respectively, and *CO_2, *COOH and *CO are the intermediates chemisorbed on

the catalysts surface. In some case, it is possible that Eqs.(S3) and (S4) are combined into one reaction:

$$* \mathrm{COOH} + \mathrm{H}^+ + e^- \rightarrow \mathrm{CO}_{(g)} + \mathrm{H_2O}_{(l)} \qquad (S3a)$$

Due to desorption of CO from the surface of the catalysts.

CO_2RR to CO_2H_2 product is assumed to proceed a three-step reaction:

$$* + \mathrm{CO}_{2(g)} \rightarrow * \mathrm{OCO} \qquad (S5)$$

$$* \mathrm{OCO} + \mathrm{H}^+ + e^- \rightarrow * \mathrm{OCHO} \qquad (S6)$$

$$* \mathrm{OCHO} + \mathrm{H}^+ + e^- \rightarrow \mathrm{OCHOH}_{(l)} \qquad (S7)$$

where *OCO, and *OCHO are the intermediates chemisorbed on the catalysts surface.

Hydrogen evolution reaction (HER) follows the pathway:

$$* + \mathrm{H}^+ + e^- \rightarrow * \mathrm{H} \qquad (S8)$$

$$* \mathrm{H} + \mathrm{H}^+ + e^- \rightarrow \mathrm{H}_{2(g)} \qquad (S9)$$

The free energy of elementary reactions of CO_2RR are calculated with the model of computational hydrogen electrode (CHE).[1] Briefly, the Gibbs free energy change of each elementary step of CO_2RR is calculated with the density functional theory (DFT). Accordingly, the chemical potential of the solvated proton and electron pair ($H^+ + e^-$) at standard conditions is equal to half of the gaseous hydrogen ($1/2G_{H2}$) at the standard hydrogen electrode. The corrections, such as zero-point energy (ΔE_{ZPE}), heat capacity (ΔC_p), temperature (T) and entropy (ΔS), together with the DFT total energy (ΔE_{DFT}), are considered in calculating the free energy (ΔG) of each elementary reaction, which takes the formula[2]:

$$\Delta G = \Delta E_{DFT} + \Delta E_{ZPE} + \int C_p d_T - T\Delta S + eU_{SHE} \qquad (S10)$$

where ΔE_{ZPE}, C_p, and ΔS are calculated from statistical mechanics within the harmonic approximation, taking the vibrational frequencies of adsorbates and molecules as calculated within DFT. These correction values of different adsorbate species are exhibited in Table S1. The energy of these elementary steps (ΔE_{DFT}) is the energy differences between the DFT-calculated energies of the product and reactant states. In this work, ΔE_{DFT}, calculated from the double reference method (DRM), is potential-dependent. The correction of applied voltage (eU_{SHE}) is incorporated in the Gibbs free energy calculation of each electrochemical step. Moreover, an

addition value of -0.51 eV is added into CO gaseous molecules to correct the large deviations from the standard value in using GGA-PBE functional.[3] For the CO_2RR catalytic mechanism, the equilibrium potentials at standard conditions are -0.12 V/SHE and -0.20 V/SHE for products, CO and HCOOH, respectively.[4]

The adsorption energy of intermediates in CO_2RR is calculated by:

$$\Delta G_{*CO2} = G_{*CO2} - G_* - G_{CO2} \quad (S11)$$

$$\Delta G_{*COOH} = G_{*COOH} - G_* - (G_{CO2} + 1/2G_{H2}) \quad (S12)$$

$$\Delta G_{*CO} = G_{*CO} - G_* - (G_{CO2} + G_{H2} - G_{H2O}) \quad (S13)$$

where G_* is the ground state energy of clean catalysts, G_{*CO2}, G_{*COOH} and G_{*CO} are the ground state energies of the catalysts absorbed with *CO_2, *COOH, and *CO adsorbates, respectively. The energies of G_*, G_{*CO2}, G_{*COOH} and G_{*CO} are calculated from the DRM, which are potential-dependent. G_{CO2}, G_{H2} and G_{H2O} are the energies of CO_2, H_2 and H_2O gaseous/liquid molecules, respectively.

The rate-limiting potential of CO_2RR is calculated by:

$$U_L = max\{\Delta G_1, \Delta G_2, \Delta G_{3a}\}/e \quad (S14)$$

$$U_L = max\{\Delta G_1, \Delta G_2, \Delta G_3, \Delta G_4\}/e \quad (S15)$$

where ΔG_1, ΔG_2, ΔG_3, ΔG_4 and ΔG_{3a} are the free energy change of Reaction S1-S4 and S3a calculated by Eq. (S10), respectively. For HER in Eqs. S8-S9,

$$U_L = max\{\Delta G_1, \Delta G_2\}/e \quad (S16)$$

Note 2. Spin-orbit interaction

The spin-orbit interaction (or spin Hall effect) is derived from the electron spin-polarization, namely the electromagnetic interaction between the electron's magnetic dipole and the electrostatic field.[5] As schematically illustrated in Figure S10a, there is a longitudinally generating spin currents under the transverse external current (charge current).[6] Since there is the interaction of the spin-orbital coupling between the charge flow and the spin current (the coupling between the spin and the orbit will produce different deflection effects on the electrons of different spins), it leads to a shift in their energy levels, as illustrated in Figure S10b.[7]

In our calculations, we demonstrated that the Ni d_{x2-y2} energy level above the Fermi level has a significant split with the increase of the applied voltage, as shown in Figure S11. It could be explained by the fact that the applied external potential promotes charge transfer, inducing the

current density between the intermediates and substrate in the *z* direction, as well as the electrons in *x*-*y* plane. Thus, the spin-orbit interaction occurs, producing newly energy levels, and partially occupied d_{x2-y2} orbitals below the Fermi level, as shown in Figure S11. This phenomenon of spin-orbit interaction is occasionally observed in experiments with electrochemical reactions.[8, 9, 10] Therefore, we propose that the *d* electrons at *z*-direction energy level play a critical role in the adsorption of CO_2 and its intermediates since the obviously overlapping between d_{z2} (or d_{xz}, d_{yz}) orbitals of Ni atom and π* anti-bonding orbitals of CO_2 adsorbate to form *d*-π* (occ) and *d*-π* (unocc) hybridized energy levels,[4] while the *d* electrons at *x*-*y* plane, including d_{x2-y2} and d_{xy}, act as a bridge to connect the orbitals of *d*-π* (occ) and *d*-π* (unocc), making the *d* electrons of Ni atom conveniently transferrable to the $*CO_2$ adsorbates.

Note 3. Solvent Impact in Electrochemical CO_2RR

In addition to the applied voltage, the solvent impact also plays an irreplaceable role in both stabilizing adsorption configuration of the intermediate and enhancing their adsorption strength, confirmed by previous articles[11].

In order to gain deep insights into the solvent impact, we performed comparison calculations with the DRM models (i) without considering solvent effects; ii) Only using the implicit solvent model to simulate the long-term solvent impact; iii) Utilizing both the implicit and explicit models (two H_2O molecules around per adsorbate) to simulate the long-term and local solvent effects of aqueous solution. It is worth noting that the elementary reaction of $*CO_2$ chemisorption usually determines the activity of the electrocatalyst, so here we only discuss the influence of the solvent effect on the $*CO_2$ adsorbent. Figure S13-17 demonstrated the simulation results of the above three cases. The results show that the applied voltages to trigger $*CO_2$ chemisorption are respectively identified as -1.26 V, -1.06 V and -0.82 V for these three cases, which are far from the experimental results (-0.50 V). Therefore, these three comparison calculations fail to reproduce the onset-potential in experiments. By contrast, the implicit and explicit models (four H_2O molecules around per adsorbate) we adopted in this work have successfully predict the catalytic behavior of CO_2RR on Ni-N_4 SAC, including CO_2 chemisorption, onset-potential, and product selectivity. It should be noted that we did not attempt to add more explicit water molecules (e.g., six or eight H_2O molecules per adsorbate) to the system since the existence of geometric steric hindrance prevents the intermediate from obtaining more hydrogen bonds. The optimal

configurations with four H_2O molecules around the adsorbates have been supported by the report describing the role of hydrogen bonding in electrochemical CO_2 reduction[12].

Note 4. Electrocatalyst synthesis

The Ni@NCH and Fe@NCH electrocatalysts were prepared *via* a polymerization-calcination strategy combined with silica-templating. Specifically, 0.5 mL of ammonia solution (NH_4OH, Sigma Aldrich, 35%) was injected into a mixed solution containing ethanol (12 mL) and DI water (40 mL). Subsequently, 1 mL of tetraethyl orthosilicate (TEOS, Sigma Aldrich, 99.99%) was dropwise added into the above solution and kept stirring for 10 min to form SiO_2 suspension, followed by addition of 0.1 mmol nickel nitrate ($Ni(NO_3)_2•6H_2O$, Sigma Aldrich, 99.99%). Then, 3 mL of dopamine hydrochloride solution ($C_8H_{12}ClNO_2$, Sigma Aldrich, 0.26 M, 98%), which was used as the nitrogen-doped carbon precursor, were quickly injected into the above suspension, and the self-polymerization was spontaneously triggered. After 48 h later, the precipitates were collected by centrifuging, washed with DI water several times and dried at 80°C in an oven. The obtained powder was then subjected to a calcination treatment under an argon atmosphere at 800°C. To remove the silica template, alkaline leaching (2 M NaOH) was carried out at 90°C for 4 h after annealing. The samples were then acid washed (0.5 M H_2SO_4) at 90°C for 4 h. The acid-washed samples were calcined again at the same conditions.

Note 5. Electrochemical methods

All working electrodes were prepared by dissolving 2 mg of catalyst powder in 1.0 mL of DI water and ethanol solution (1:1, v/v) followed by the addition of 30 µL of Nafion solution (Sigma-Aldrich, 99.99%). The resulting mixture was ultrasonicated to form a homogeneous ink, which was then drop cast on Teflon-lined carbon fiber paper to attain a catalyst loading of 0.5 mg/cm^2. Electrochemical measurements (unless mentioned otherwise) in this study were carried out with an Autolab M204 (Metrohm Autolab) electrochemical workstation, using a customized glass frit separated two-compartment gas-tight H-cell. The cathode compartment of the H-cell contained the Ni/Fe electrodes and a saturated calomel electrode (SCE) as the working and reference electrode respectively, whereas the anode compartment contained a Pt wire as the counter electrode. 0.1 M $KHCO_3$ was utilized in this study as the electrolyte. Before each experiment, the cathodic compartment of the H-cell was purged with CO_2 for 30 minutes, and the CO_2 saturated 0.1 M $KHCO_3$ solution gave a pH measurement of 6.8. All potentials measured in

this study were converted to the reversible hydrogen electrode (RHE) reference using the following equation: E^{RHE} (V) = E^{SCE} (V) + 0.245 + 0.059 × pH. Constant potential electrolysis (without iR compensation) was carried out at various potentials for one hour and the experiments were repeated three times, and the results presented are the averaged values.

Note 6. Product detection

A gas chromatograph (Shimadzu, Model 2010 Plus), equipped with both thermal conductivity detector (TCD) and flame ionization detector (FID) detectors, was used to quantify the gas-phase products after 1800s and 3600s during the one-hour long bulk electrolysis. 0.5 mL of liquid aliquots were collected at the end of each experiment and mixed with 0.1 mL of D_2O and 7.143 ppm of internal standard dimethyl sulfoxide (DMSO, Sigma 99.99%), and were analyzed using a 600 MHz ^{1}H 1 D liquid NMR spectrometer (Bruker Advance) at 25 °C. The 1D ^{1}H spectrum was measured with water suppression with a pre-saturation method.

Supplementary Figures

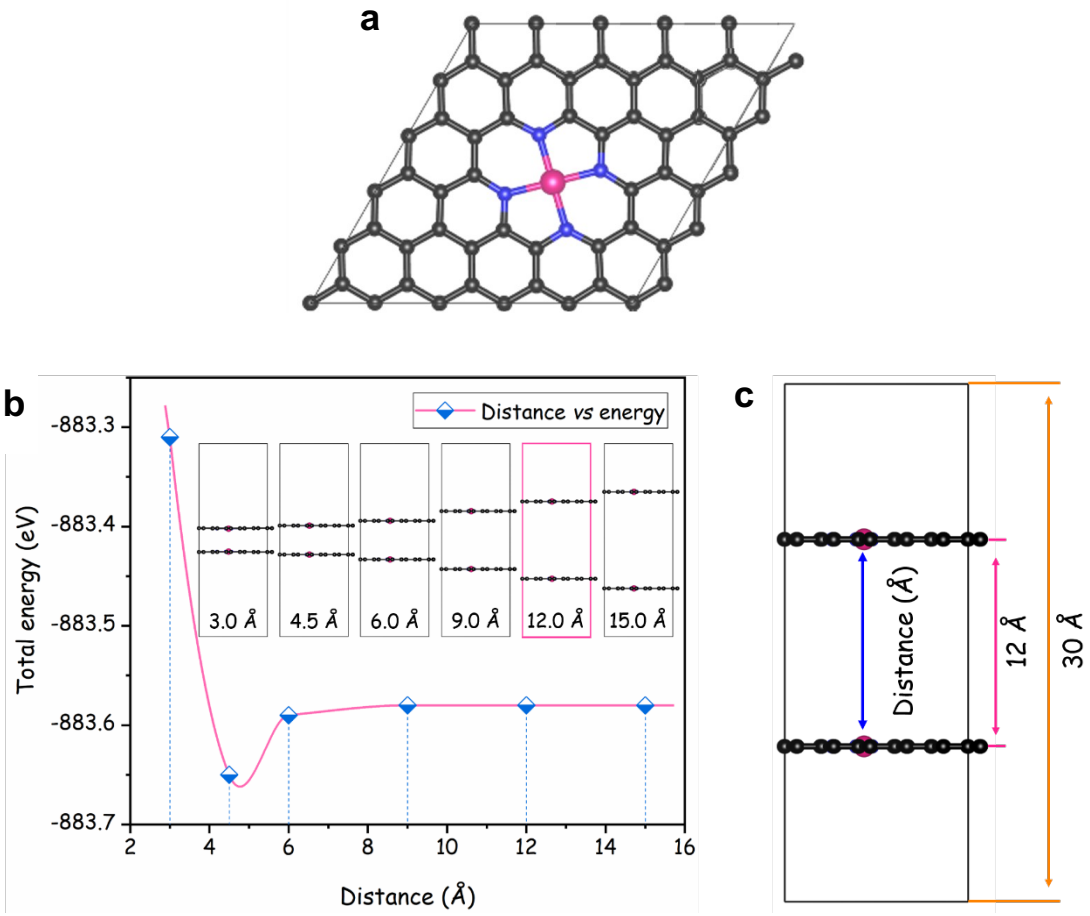

Figure S1. (a) Schematic of transition metal TM-N_4 SAC. (b) The total energy of Ni-N_4 SAC as a function of the distance (Å) in *z*-direction between those two layers in a periodic unit. (c) The geometry structure chosen in this work, where the distance between two layers was set to 12 Å, and the lattice size in *z*-direction was set to 30 Å to reserve an 18 Å vacuum spacing between the periodically repeated images, such that the artificial interactions and electric dipoles in the system can be eliminated.

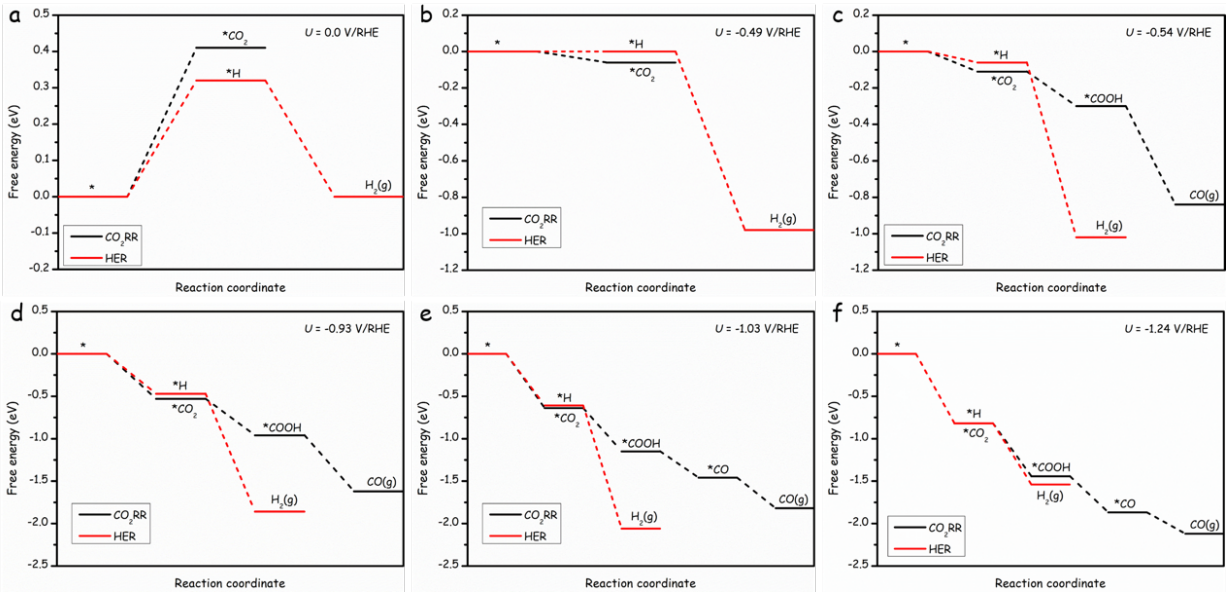

Figure S2. Free energy diagrams of CO_2RR and HER on Ni-N_4 SAC at typical applied voltages. (a) U = 0 V/RHE, (b) U = –0.49 V/RHE, (c) U = –0.54 V/RHE, (d) U = –0.93 V/RHE, (e) U = –1.03 V/RHE, and (f) U = –1.24 V/RHE. There are several catalytic pathways depending on the applied potential:

0 ~ –0.49 V: Neither CO_2RR nor HER occurs due to unstable chemisorption of CO_2 and H at the active site (adsorption free energies of both CO_2 and H are positive);

–0.49 ~ –0.54 V: HER proceeds but CO_2RR does not;

–0.54 ~ –0.93 V: CO_2RR starts and becomes preferrable over HER because of its lower free energy (ΔG_L), thus the Faraday Efficiency (FE^{CO}) increases rapidly;

–0.93 ~ –1.24 V: ΔG_L of HER becomes lower than that of CO_2RR, indicating the FE^{CO} achieves its maximum value at –0.93 V and then decreases sluggishly. In this regime, the adsorption energy of *CO_2 (ΔG_{*CO2}) is still larger than that of *H (ΔG_{*H}), which means *CO_2 is favorable to adsorb at the active sites and CO_2RR still dominates the reactions ($FE^{CO} > FE^{H2}$);

–1.24 ~ –2.00 V: both ΔG_L for HER and ΔG_{*H} are more negative, thus HER will regain its domination in the reactions.

–1.03 ~ –2.00 V: CO stably adsorbs on the surface of the Ni-N_4 SAC surface, and the corresponding catalytic mechanism of CO_2RR has become: * → *CO_2 → *COOH → *CO → CO(g);

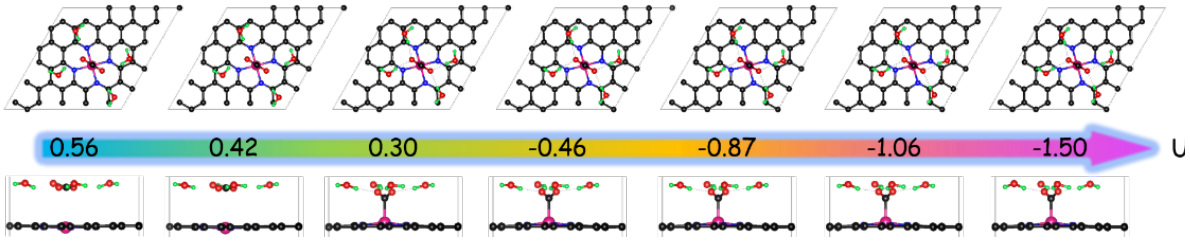

Figure S3. The structural configurations of CO_2 molecules being adsorbed on Fe-N_4 SAC surface under different applied potentials. The black, green, red and pink balls are carbon, hydrogen, oxygen and nickel atoms. respectively.

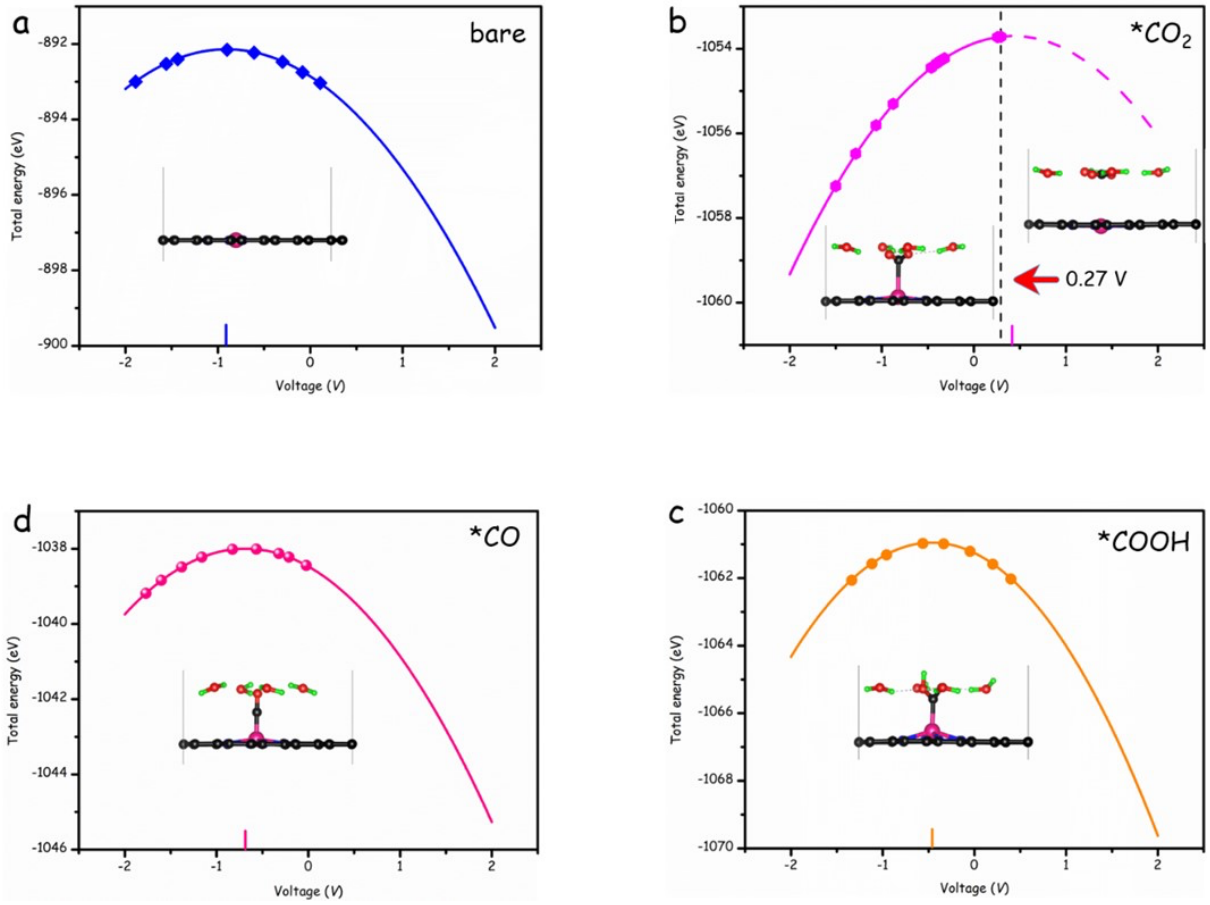

Figure S4. The total energies of clean substrate and adsorbates of CO_2RR on Fe-N_4 SAC as a function of the applied potential *U*. (a) no adsorption, (b) *CO_2, (c) *COOH, and (d) *CO. The calculated total energies are represented by the points, and the parabolic curves are the fitting curves for these energies. The solid part of the parabolic curve in (b) indicates that *CO_2 adsorbates are chemisorbed on the surface, while the dashed part represents physisorption. The insets are the structural configurations of bare, *CO_2, *COOH and *CO, respectively. The black, green, red and pink balls are carbon, hydrogen, oxygen and iron atoms, respectively.

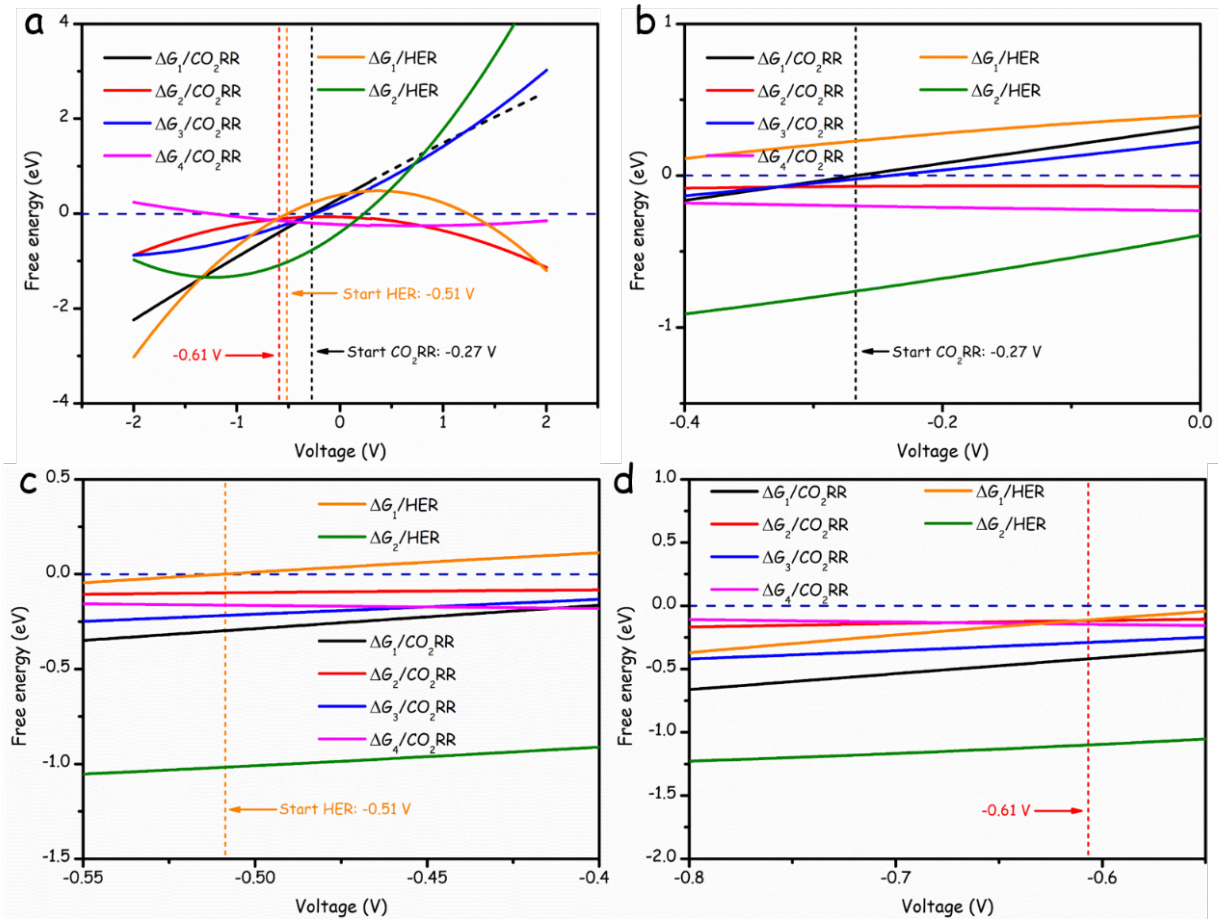

Figure S5. (a) Schematic plot of potential-dependent free energy of CO_2RR and HER on Fe-N_4 SAC; (b-d) Free energy of CO_2RR and HER as a function of applied potential (*U*/RHE) at different regimes.

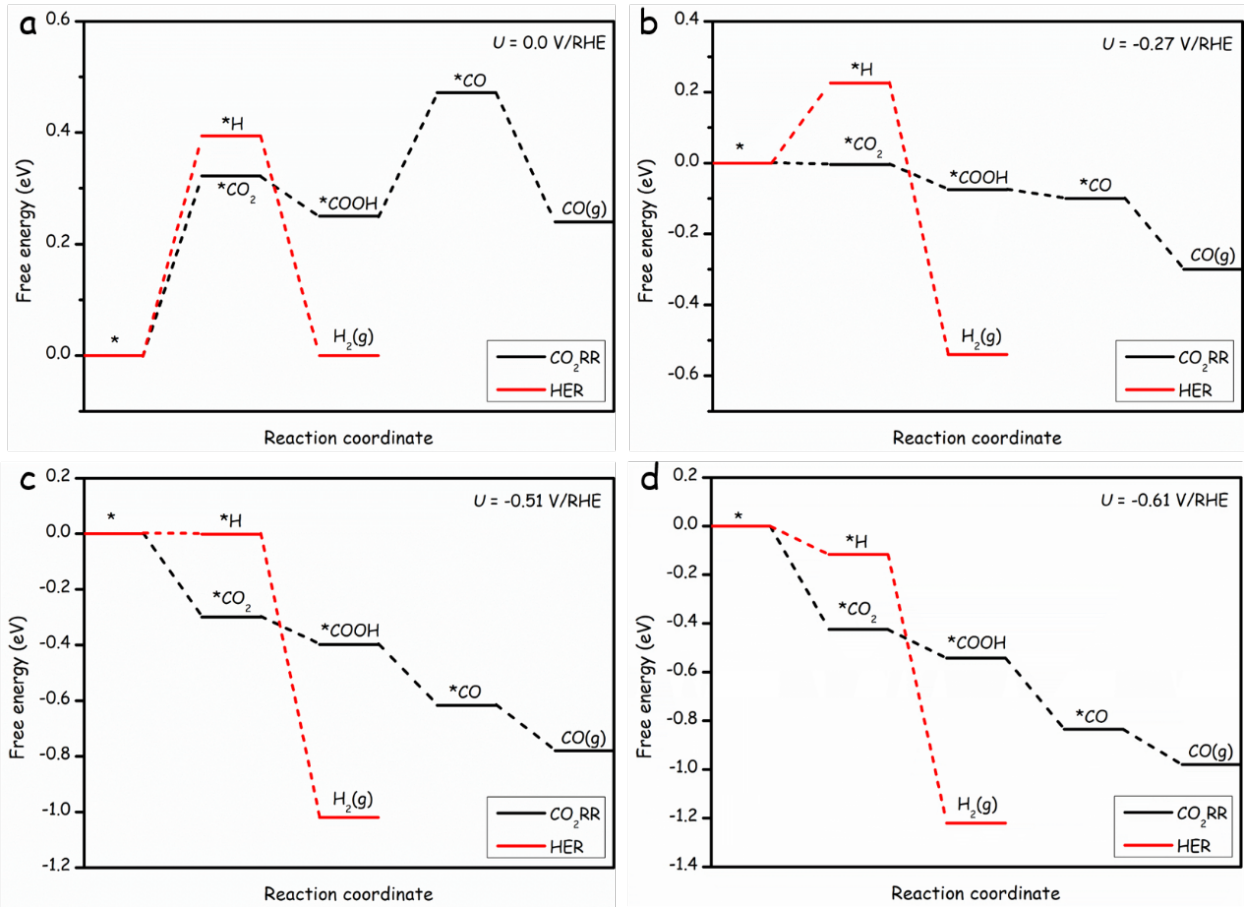

Figure S6. Free energy diagrams of the CO_2RR and HER on Fe-N_4 SAC at (a) U = 0 V/RHE, (b) U = –0.27 V/RHE, (c) U = –0.51 V/RHE, and (d) U = –0.61 V/RHE. There are several catalytic pathways depending on the applied potential U:

0 ~ –0.27 V: both CO_2RR and HER did not occur due to the positive free energy;

–0.27 ~ –0.51 V: CO_2RR proceeds but HER is still inactive;

–0.51 ~ –0.61 V: CO_2RR is more active than HER due to its lower RLS free energy (ΔG_L). Thus the Faraday Efficiency (FE^{CO}) increases rapidly;

–0.61 ~ –2.00 V: ΔG_L of HER was lower than that of CO_2RR, indicating the FE^{CO} achieved a maximum value at –0.61 V and then decrease sluggishly.

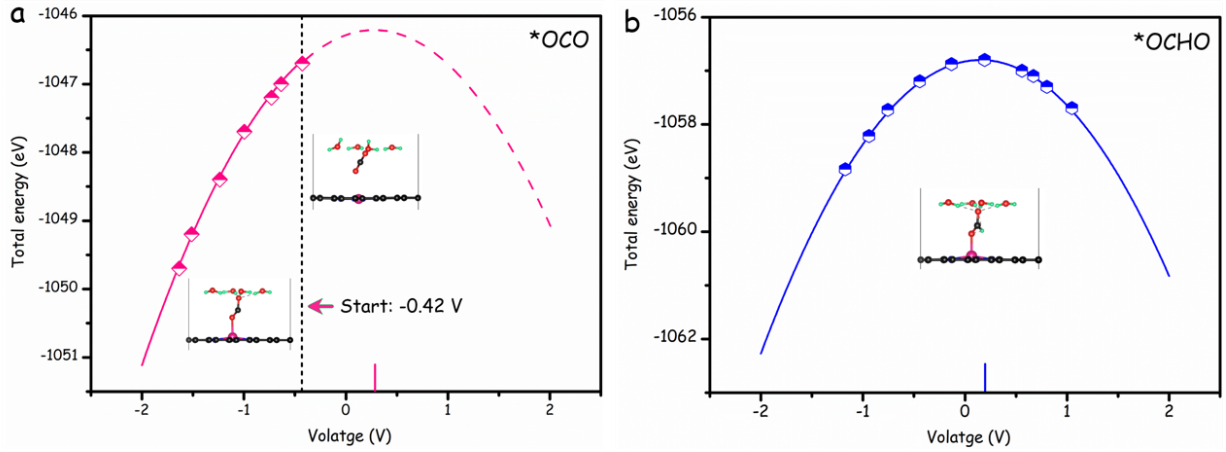

Figure S7. The total energies of (a) *OCO and (b) *OCHO intermediates on Ni-N_4 SAC as a function of the applied potential *U*. The calculated total energies are distinguished as the points in the corresponding diagrams, and the polynomial fits to these energies are the parabolic curves. The solid part of the parabolic curve in (a) indicates that the *OCO adsorbates was chemisorbed on the surface, while the dashed part was away from the surface. The insets are the structural configurations of *OCO and *OCHO. The black, green, red and pink balls are carbon, hydrogen, oxygen and nickel atoms, respectively.

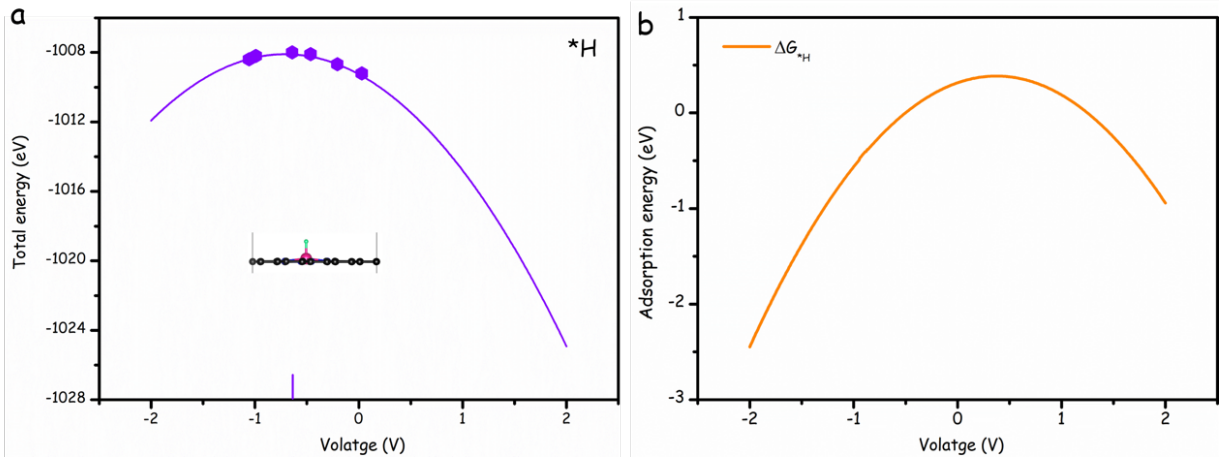

Figure S8. (a) The total energies of *H adsorbate on Ni-N_4 SAC as a function of the applied potential *U*. The calculated total energies are represented by the points, and the parabolic curves are the results of polynomial fitting to these energies. The insets are the structural configuration of *H, and the black, green and pink balls are carbon, hydrogen and nickel atoms, respectively. (b) The adsorption energy of *H adsorbate (ΔG_{*H}) as a function of applied potential.

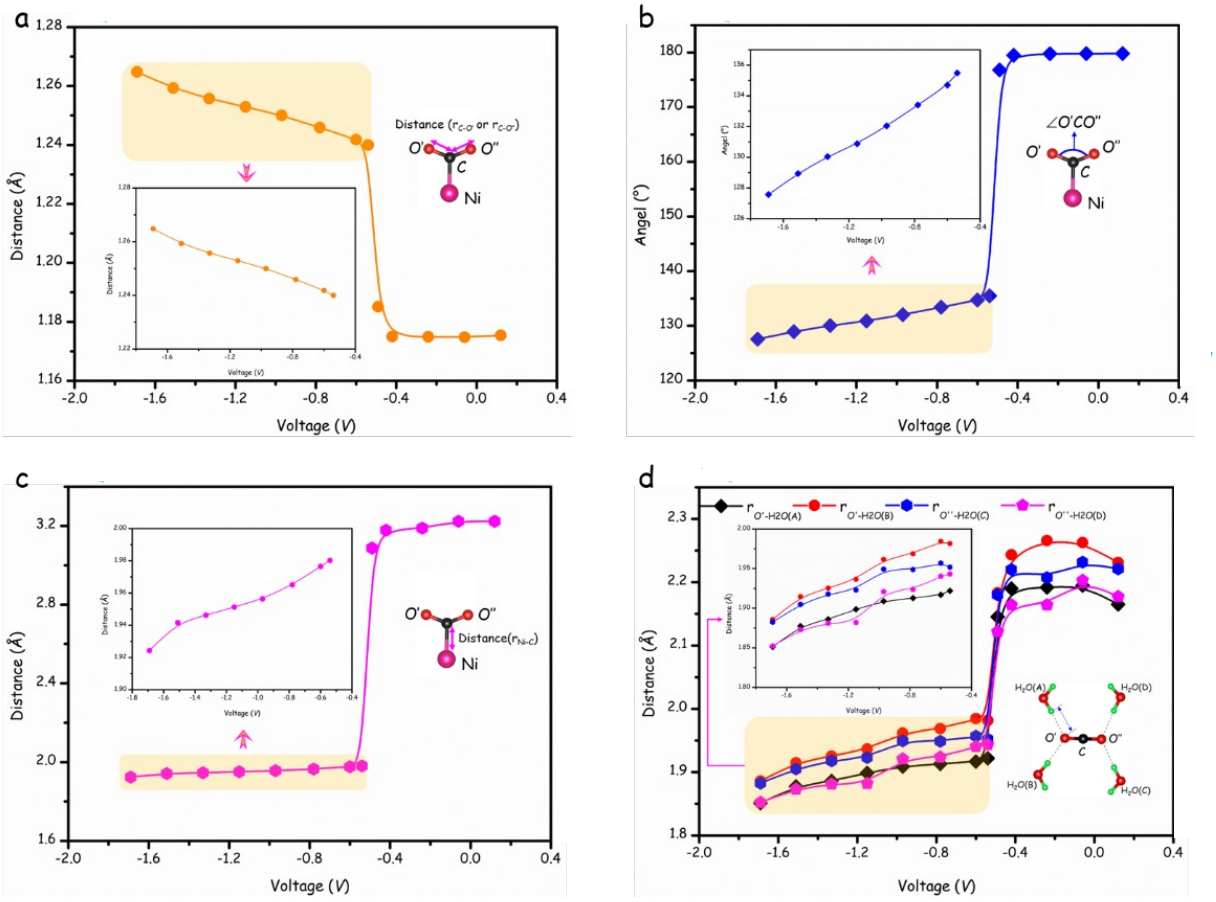

Figure S9. The potential-dependent variations of *CO_2 geometric configuration, involving: (a) the distance of C-O′ ($r_{C\text{-}O'}$) or C-O″ ($r_{C\text{-}O''}$) in CO_2 adsorbates; (b) the angel of $\angle OCO$ in CO_2 adsorbates; (c) the distance between Ni atom and CO_2 ($r_{Ni\text{-}C}$); and (d) the hydrogen bond strength between CO_2 and surrounding H_2O molecules. The insets are the variations of the *CO_2 geometric configuration after being chemisorbed on the surface

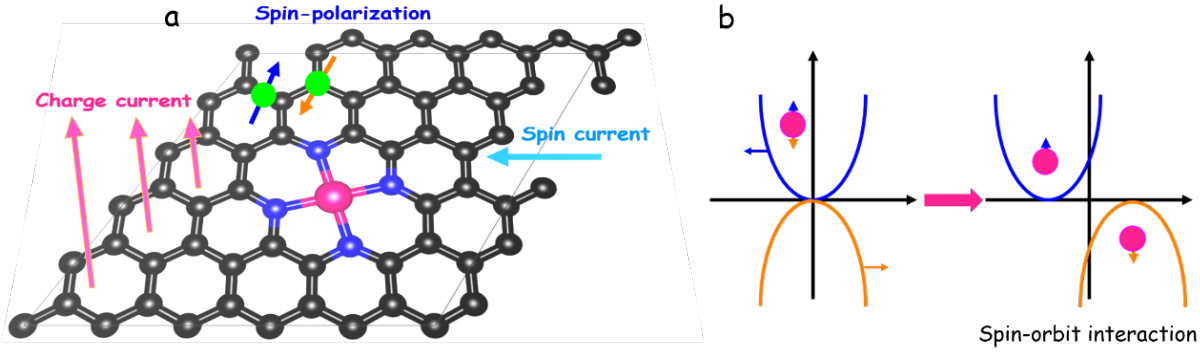

Figure S10. The schematic diagrams of (a) spin-orbit interaction (or spin Hall effect) on carbon-based catalyst, and (b) spin-orbit interaction leads to a shift in energy levels.

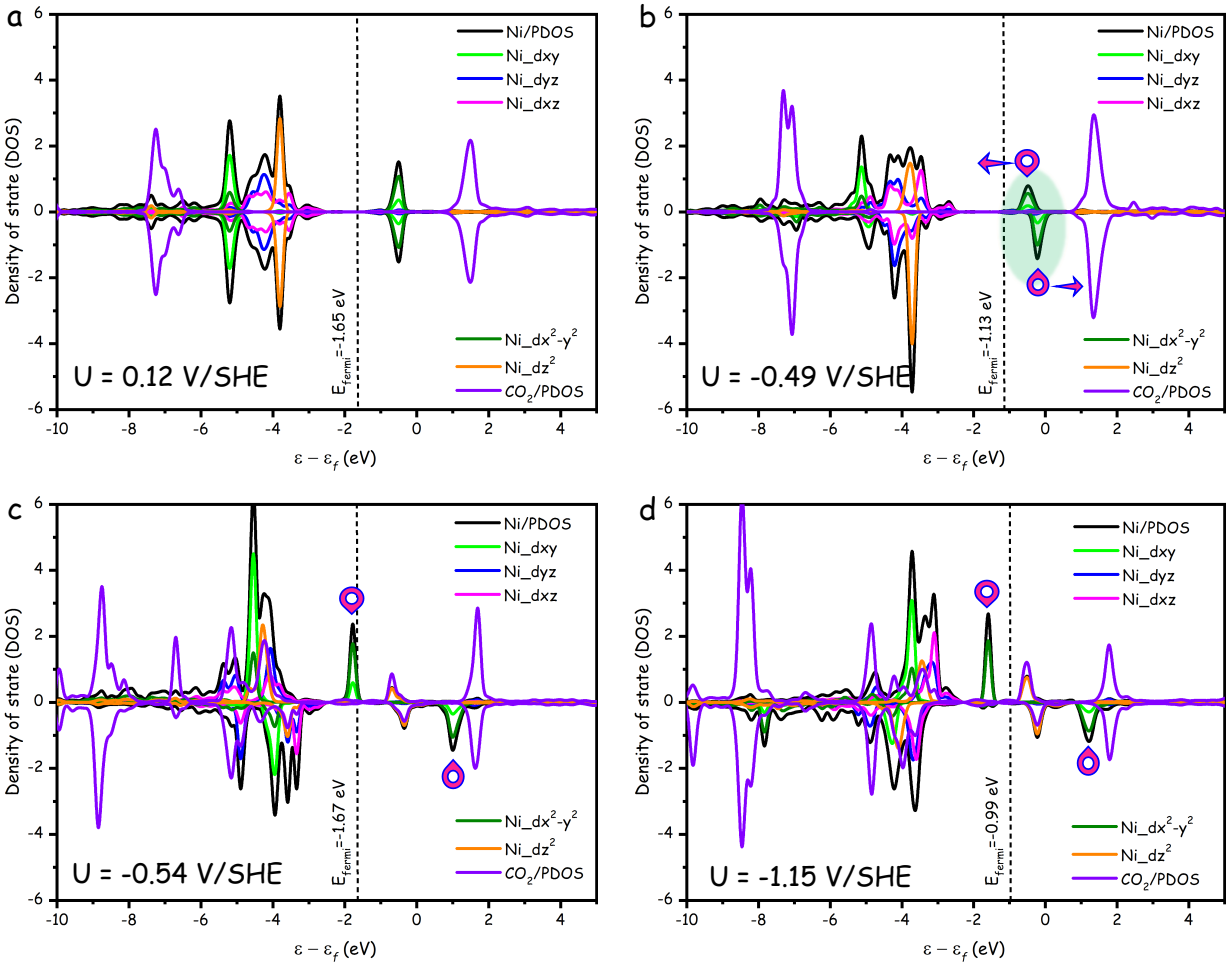

Figure S11. The projected density of state of Ni atom (Ni/PDOS, black) and its *d* orbitals (d_{xy}/green, d_{yz}/blue, d_{xz}/magenta, $d_{x2\text{-}y2}$/olive, d_{z2}/orange), as well as the CO_2 adsorbate (CO_2/PDOS, violet) under different applied potential, including: (a) U = 0.12 V/SHE; (b) U = –0.49 V/SHE; (c) U = –0.54 V/SHE; and (d) U = –1.15 V/SHE.

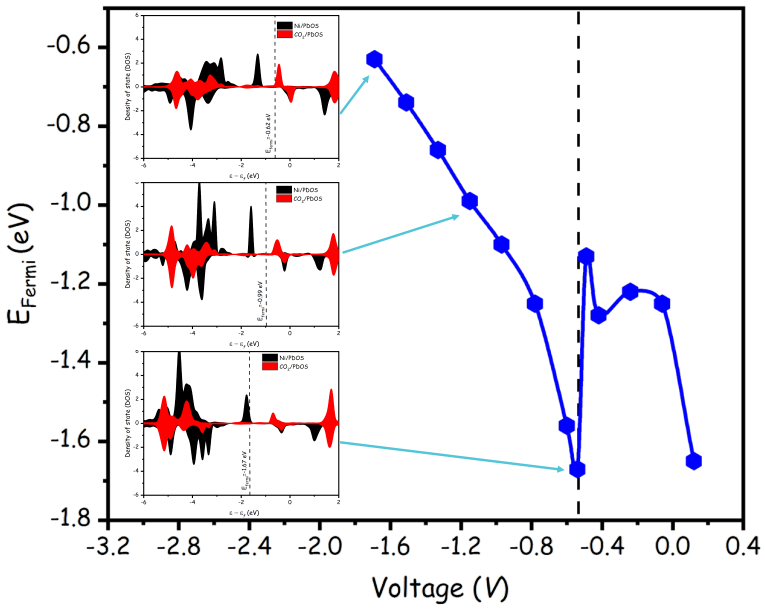

Figure S12. The Fermi level (E_{Fermi}/eV) as a function of the applied potential (V). The insets are the PDOS of Ni (black) and CO_2 (red) *via* Fermi level under different voltages.

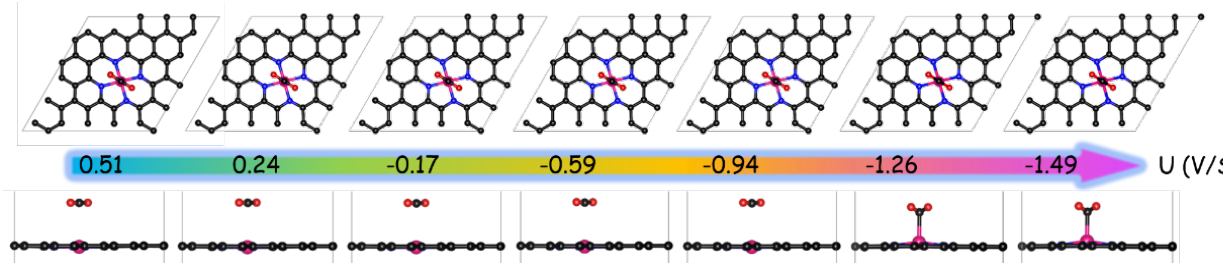

Figure S13. The structural configurations of CO_2 molecules adsorbed on Ni-N_4 SAC surface under different applied potentials, calculated using the DRM approach that do not consider solvent effects. The black, green, red and pink balls are carbon, hydrogen, oxygen and nickel atoms, respectively.

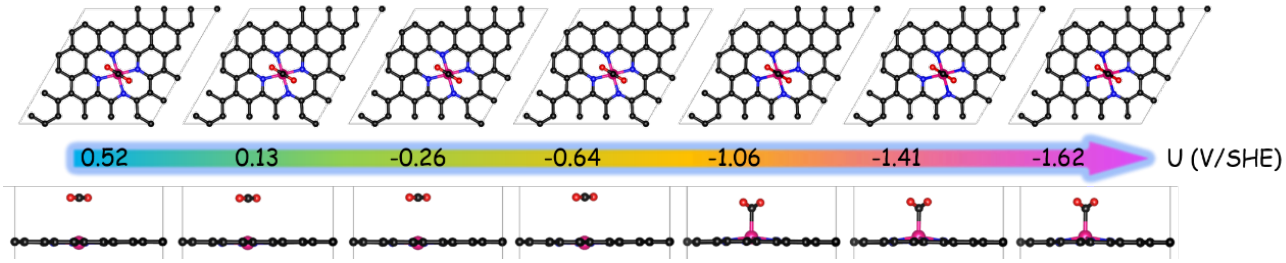

Figure S14. The structural configurations of CO_2 molecules adsorbed on Ni-N_4 SAC surface under different applied potentials, calculated using the implicit solvent model. The black, green, red and pink balls are carbon, hydrogen, oxygen and nickel atoms, respectively.

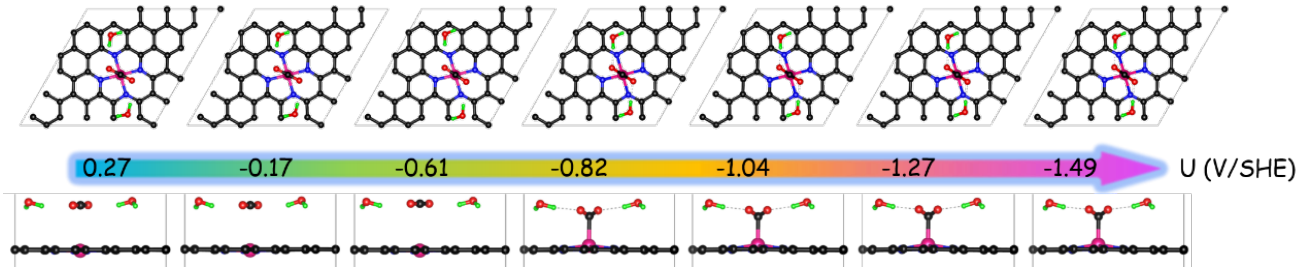

Figure S15. The structural configurations of CO_2 molecules adsorbed on the Ni-N_4 SAC surface under different applied potentials. The calculations were made using both the implicit solvent and explicit model (two H_2O molecules around the adsorbates were added into the system). The black, green, red and pink balls are carbon, hydrogen, oxygen and nickel atoms, respectively.

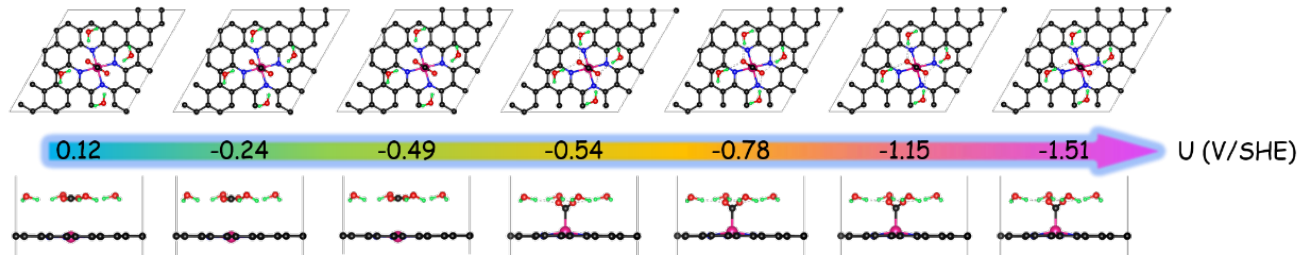

Figure S16. The structural configurations of CO_2 molecules adsorbed on the Ni-N_4 SAC surface under different applied potential. The calculations were made utilizing both the implicit solvent and explicit model (four H_2O molecules around the adsorbates were added into the system). The black, green, red and pink balls are carbon, hydrogen, oxygen and nickel atoms, respectively.

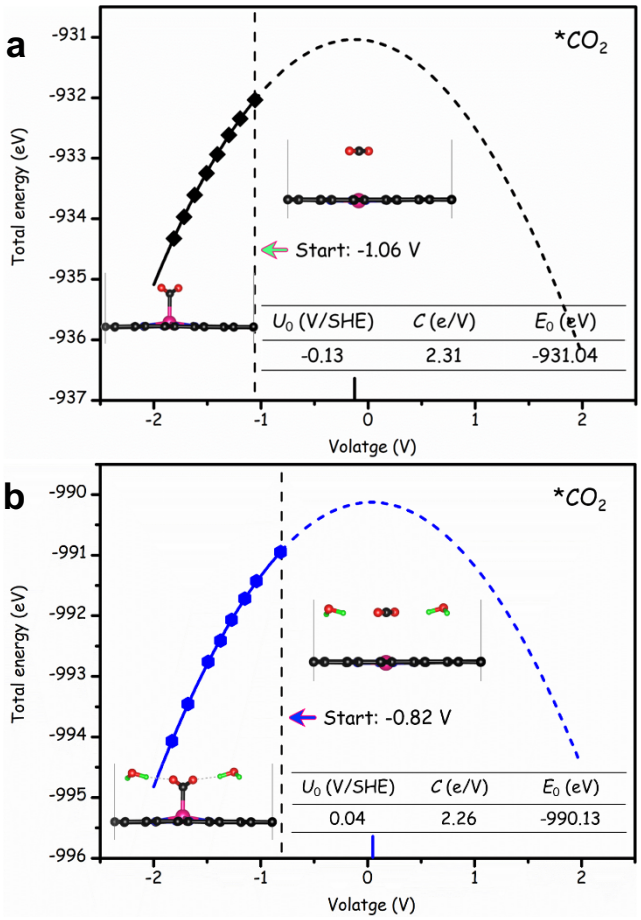

Figure S17. The total energies of *CO_2 intermediates on Ni-N_4 SAC as a function of the applied potential *U*, calculated using (a) the implicit solvent model, and (b) combination of the implicit solvent and explicit model (two H_2O molecules around the adsorbates). The total energies are calculated using Eq.3. The solid part of the parabolic curve indicates that the *CO_2 adsorbates was chemisorbed on the surface, while the dashed part was away from the surface. The insets are the structural configurations of *CO_2. The black, green, red and pink balls are carbon, hydrogen, oxygen and nickel atoms, respectively.

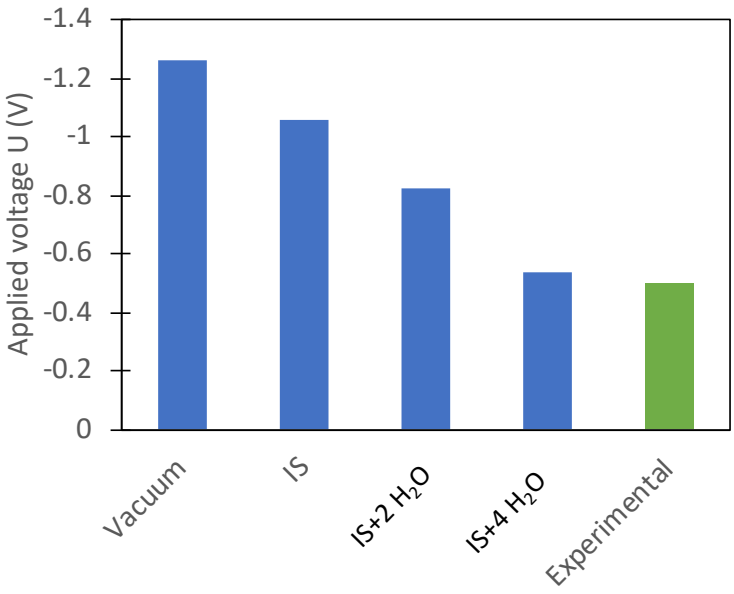

Figure S18. The critical applied voltage at which CO_2 adsorbs on Ni-N_4 SAC under different environments (vacuum, IS (implicit solvent), IS + two H_2O molecule, IS + four H_2O molecules), and onset potential measurement.

Supplementary Tables

Table S1. Corrections including zero-point energy (ΔE_{ZPE}), heat capacity (ΔC_p) and entropy (ΔS) at 298.15K for calculation of total energy to Gibbs free energy (ΔG) (eV).

Adsorbate	ΔE_{ZPE}	$T\Delta S$	$\int C_p dT$	$\Delta E_{ZPE} + \int C_p d_T - T\Delta S$
*CO_2	0.32	0.19	0.12	0.25
*OCO	0.30	0.16	0.09	0.23
*COOH	0.61	0.18	0.08	0.51
*OCHO	0.62	0.20	0.10	0.52
*CO	0.19	0.09	0.06	0.16
*OCHOH	0.82	0.09	0.05	0.78
CO_2	0.31	0.65	0.10	-0.24
CO	0.14	0.67	0.09	-0.44
HCOOH	0.90	1.02	0.11	-0.01
H_2O	0.58	0.65	0.10	0.03
H_2	0.27	0.42	0.09	-0.06

Table S2. Fitted parameters of the quadratic equation for the total energies of CO_2RR and HER species on Ni-N_4 SACs.

Species	U_0 (V/SHE)	C (e/V)	E_0 (eV)
bare	-0.86	2.09	-887.21
*CO_2	0.14	2.33	-1048.59
*OCO	0.26	1.92	-1046.20
*COOH	-0.35	3.32	-1055.60
*OCHO	0.15	2.36	-1056.80
*CO	-0.35	2.62	-1032.01
*H	-0.71	3.89	-1008.10

Table S3. Fitted parameters of the quadratic equation for the total energies of various CO_2RR and HER species on Fe-N_4 SAC.

Species	U_0 (V/SHE)	C (e/V)	E_0 (eV)
bare	-0.91	1.75	-892.14
*CO_2	0.42	1.91	-1053.70
*COOH	-0.46	2.86	-1060.90
*CO	-0.68	2.02	-1038.00
*H	-0.63	4.26	-898.43

Table S4. The experimental results of electrocatalytic CO_2RR on Ni-N_4 and Fe-N_4 SACs, including their onset-potential, maximum Faraday efficiency (FE^{CO}) and corresponding potential, and electrolyte.

	Catalyst	Onset-potential	Maximum FE^{CO}		Electrolyte
Ni-N_4	Ni@NCH-800[13]	–0.50 V	72%	–0.90 V	0.1 M $KHCO_3$
	Ni@NC-800[14]	–0.50 V	93%	–0.90 V	0.1 M $KHCO_3$
	Ni SAs/N-C[15]	–0.57 V	71.9%	–0.90 V	0.5 M $KHCO_3$
	NiPor-CTF[16]	–0.55 V	97%	–0.90 V	0.5 M $KHCO_3$
	Ni-N_4-C[17]	–0.48 V	99%	–0.81 V	0.5 M $KHCO_3$
	SE Ni SAs@PNC[18]	–0.50 V	96%	–0.80 V	0.1 M $KHCO_3$
	Ni SAs/NCNTs[19]	–0.56 V	97%	–0.90 V	0.5 M $KHCO_3$
	A-Ni-NG[20]	–0.50 V	97%	–0.90 V	0.5 M $KHCO_3$
	Ni-N-Gr[21]	–0.58 V	92%	–0.90 V	0.1 M $KHCO_3$
	Ni SAs/F-CPs[22]	–0.50 V	86%	–0.90 V	0.5 M $KHCO_3$
	Ni SAs/CFPs[22]	–0.50 V	96%	–0.90 V	0.5 M $KHCO_3$
	Ni-CNT-CC[23]	–0.50 V	99%	–0.78 V	0.5 M $KHCO_3$
	Ni-PANI[24]	N/A	85%	–0.90 V	0.1 M $KHCO_3$
	NiSA/PCFM[25]	N/A	88%	–1.00 V	0.5 M $KHCO_3$

	SA-Ni/N-CS[26]	N/A	91.5%	–0.80 V	0.5 M $KHCO_3$
	Ni@NCH (This work)	–0.50 V	79.1%	–0.90 V	0.1 M $KHCO_3$
	Ni-N_4-C* (This work)	–0.54 V*	N/A	–0.93 V*	N/A
Fe-N_4	NFe-CNT/CNS[27]	–0.30 V	69%	–0.59 V	0.1 M $KHCO_3$
	Fe-N-C[28]	–0.30 V	95.3%	–0.60 V	0.1 M $KHCO_3$
	H-M (FeN_4)[29]	–0.26 V	69%	–0.56 V	0.1 M $KHCO_3$
	FeN_4/C[30]	–0.30 V	93%	–0.60 V	0.1 M $KHCO_3$
	FeSAs/PTF[31]	–0.11 V	67%	–0.60 V	0.5 M $KHCO_3$
	Fe-N-C[32]	–0.25 V	89%	–0.59 V	0.1 M $KHCO_3$
	Fe-NPCA[33]	–0.30 V	78%	–0.60 V	0.1 M $KHCO_3$
	Fe-N-C[24]	N/A	76%	–0.61 V	0.1 M $KHCO_3$
	Fe-N-C[34]	–0.29 V	93%	–0.59 V	0.1 M $KHCO_3$
	Fe@NCH (This work)	–0.30 V	73.5%	–0.60 V	0.1 M $KHCO_3$
	Fe-N_4-C* (This work)	–0.27 V*	N/A	–0.61 V*	N/A

* represents the theoretical results calculated by DRM approach.

Supplementary References

1. Hansen HA, Varley JB, Peterson AA, Nørskov JK. Understanding Trends in the Electrocatalytic Activity of Metals and Enzymes for CO_2 Reduction to CO. *The Journal of Physical Chemistry Letters* **4**, 388-392 (2013).

2. Hirunsit P. Electroreduction of Carbon Dioxide to Methane on Copper, Copper–Silver, and Copper–Gold Catalysts: A DFT Study. *The Journal of Physical Chemistry C* **117**, 8262-8268 (2013).

3. Chai G-L, Guo Z-X. Highly effective sites and selectivity of nitrogen-doped graphene/CNT catalysts for CO_2 electrochemical reduction. *Chemical Science* **7**, 1268-1275 (2016).

4. Gong L*, et al.* Catalytic mechanism and design principle of coordinately unsaturated single metal atom-doped covalent triazine frameworks with high activity and selectivity for CO_2 electroreduction. *Journal of Materials Chemistry A* **9**, 3555-3566 (2021).

5. Bernevig BA, Zhang S-C. Quantum Spin Hall Effect. *Physical Review Letters* **96**, 106802 (2006).

6. McGlynn E. Electron Paramagnetic Resonance of Transition Ions, Oxford Classic Texts in the Physical Sciences, by A. Abragam and B. Bleaney. *Contemporary Physics* **54**, 115-116 (2013).

7. Hirsch JE. Spin Hall Effect. *Physical Review Letters* **83**, 1834-1837 (1999).

8. Han J*, et al.* Reordering d Orbital Energies of Single-Site Catalysts for CO_2 Electroreduction. *Angewandte Chemie International Edition* **58**, 12711-12716 (2019).

9. Chauhan M, Deka S. Hollow Cobalt Sulfide Nanoparticles: A Robust and Low-Cost pH-Universal Oxygen Evolution Electrocatalyst. *ACS Applied Energy Materials* **3**, 977-986 (2020).

10. Sun Y, Sun S, Yang H, Xi S, Gracia J, Xu ZJ. Spin-Related Electron Transfer and Orbital Interactions in Oxygen Electrocatalysis. *Advanced Materials* **32**, 2003297 (2020).

11. Zhang Z*, et al.* Reaction Mechanisms of Well-Defined Metal–N_4 Sites in Electrocatalytic CO_2 Reduction. *Angewandte Chemie International Edition* **57**, 16339-16342 (2018).

12. Zhao X, Liu Y. Unveiling the Active Structure of Single Nickel Atom Catalysis: Critical Roles of Charge Capacity and Hydrogen Bonding. *Journal of the American Chemical*

Society **142**, 5773-5777 (2020).

13. Daiyan R*, et al.* Transforming active sites in nickel–nitrogen–carbon catalysts for efficient electrochemical CO_2 reduction to CO. *Nano Energy* **78**, 105213 (2020).

14. Daiyan R*, et al.* Antipoisoning Nickel–Carbon Electrocatalyst for Practical Electrochemical CO_2 Reduction to CO. *ACS Applied Energy Materials* **2**, 8002-8009 (2019).

15. Zhao C*, et al.* Ionic Exchange of Metal–Organic Frameworks to Access Single Nickel Sites for Efficient Electroreduction of CO_2. *Journal of the American Chemical Society* **139**, 8078-8081 (2017).

16. Lu C*, et al.* Atomic Ni Anchored Covalent Triazine Framework as High Efficient Electrocatalyst for Carbon Dioxide Conversion. *Advanced Functional Materials* **29**, 1806884 (2019).

17. Li X*, et al.* Exclusive Ni–N_4 Sites Realize Near-Unity CO Selectivity for Electrochemical CO_2 Reduction. *Journal of the American Chemical Society* **139**, 14889-14892 (2017).

18. Yang J*, et al.* In Situ Thermal Atomization To Convert Supported Nickel Nanoparticles into Surface-Bound Nickel Single-Atom Catalysts. *Angewandte Chemie International Edition* **57**, 14095-14100 (2018).

19. Lu P*, et al.* Facile synthesis of single-nickel-atomic dispersed N-doped carbon framework for efficient electrochemical CO_2 reduction. *Applied Catalysis B: Environmental* **241**, 113-119 (2019).

20. Yang HB*, et al.* Atomically dispersed Ni(I) as the active site for electrochemical CO_2 reduction. *Nature Energy* **3**, 140-147 (2018).

21. Su P, Iwase K, Nakanishi S, Hashimoto K, Kamiya K. Nickel-Nitrogen-Modified Graphene: An Efficient Electrocatalyst for the Reduction of Carbon Dioxide to Carbon Monoxide. *Small* **12**, 6083-6089 (2016).

22. Zhao C*, et al.* Solid-Diffusion Synthesis of Single-Atom Catalysts Directly from Bulk Metal for Efficient CO_2 Reduction. *Joule* **3**, 584-594 (2019).

23. Liu S*, et al.* Elucidating the Electrocatalytic CO_2 Reduction Reaction over a Model Single-Atom Nickel Catalyst. *Angewandte Chemie International Edition* **59**, 798-803 (2020).

24. Möller T*, et al.* Efficient CO_2 to CO electrolysis on solid Ni–N–C catalysts at industrial current densities. *Energy & Environmental Science* **12**, 640-647 (2019).

25. Yang H*, et al.* Carbon dioxide electroreduction on single-atom nickel decorated carbon membranes with industry compatible current densities. *Nature Communications* **11**, 593 (2020).

26. Yuan C-Z*, et al.* Semi-sacrificial template synthesis of single-atom Ni sites supported on hollow carbon nanospheres for efficient and stable electrochemical CO_2 reduction. *Inorganic Chemistry Frontiers* **7**, 1719-1725 (2020).

27. Pan F, Zhao H, Deng W, Feng X, Li Y. A novel N,Fe-Decorated carbon nanotube/carbon nanosheet architecture for efficient CO_2 reduction. *Electrochimica Acta* **273**, 154-161 (2018).

28. Mohd Adli N*, et al.* Engineering Atomically Dispersed FeN_4 Active Sites for CO_2 Electroreduction. *Angewandte Chemie International Edition* **60**, 1022-1032 (2021).

29. Zhang H*, et al.* A Graphene-Supported Single-Atom FeN_5 Catalytic Site for Efficient Electrochemical CO_2 Reduction. *Angewandte Chemie International Edition* **58**, 14871-14876 (2019).

30. Li X*, et al.* Isolated FeN_4 Sites for Efficient Electrocatalytic CO_2 Reduction. *Advanced Science* **7**, 2001545 (2020).

31. Hou Y*, et al.* Unraveling the reactivity and selectivity of atomically isolated metal–nitrogen sites anchored on porphyrinic triazine frameworks for electroreduction of CO_2. *CCS Chemistry* **1**, 384-395 (2019).

32. Pan F*, et al.* Boosting CO_2 reduction on Fe-N-C with sulfur incorporation: Synergistic electronic and structural engineering. *Nano Energy* **68**, 104384 (2020).

33. Zhong H, Meng F, Zhang Q, Liu K, Zhang X. Highly efficient and selective CO_2 electro-reduction with atomic Fe-C-N hybrid coordination on porous carbon nematosphere. *Nano Research* **12**, 2318-2323 (2019).

34. Pan F*, et al.* Unveiling Active Sites of CO_2 Reduction on Nitrogen-Coordinated and Atomically Dispersed Iron and Cobalt Catalysts. *ACS Catalysis* **8**, 3116-3122 (2018).